Journal of The Electrochemical Society, **162** (1) H23-H31 (2015)
0013-4651/2015/162(1)/H23/9/$31.00 © The Electrochemical Society

Selective Chlorine Evolution Catalysts Based on Mg-Doped Nanoparticulate Ruthenium Dioxide

Daniel F. Abbott,[a,b] Valery Petrykin,[a] Maki Okube,[c] Zdenk Bastl,[a] Sanjeev Mukerjee,[b,*] and Petr Krtil[a,,z]**

[a]*J. Heyrovský Institute of Physical Chemistry, Academy of Sciences of the Czech Republic, Prague, Czech Republic*
[b]*Department of Chemistry and Chemical Biology, Northeastern University, Boston, Massachusetts 02115, USA*
[c]*Materials and Structures Laboratory, Tokyo Institute of Technology, Midori, Yokohama 226-8503, Japan*

Nanocrystalline Mg-doped ruthenium dioxide catalysts with the formula $Ru_{1-x}Mg_xO_2$ ($0 \leq x \leq 20$) were synthesized by the spray-freezing freeze-drying technique. Synthesized materials are of nanoparticulate nature and show a single phase diffraction pattern conforming to a tetragonal oxide of the rutile structural type. Magnesium ions are not distributed homogeneously in the material, but exist in Mg-rich clusters as shown by X-ray absorption spectroscopy. The refinement of the Mg EXAFS functions for materials with low Mg content shows that the magnesium rich clusters contain Mg in a highly strained environment similar to that of the rutile-type structure. The Mg environment shifts to an ilmenite-type inclusion when Mg occupies more than 10% of all cationic positions. All Mg modified materials are active in oxygen evolution and chlorine evolution reactions. Although the Mg containing catalysts show lower overall activities compared with the non-doped ruthenia, they feature enhanced selectivity toward the chlorine evolution process, which is attributed primarily to the opening of a reaction pathway for chlorine evolution associated with presence of Mg modified active sites.

Manuscript submitted October 16, 2014; revised manuscript received November 6, 2014. Published November 18, 2014.

Understanding the electrocatalytic behavior of transition metal oxides for the oxygen evolution (OER) and chlorine evolution reactions (CER) is fundamental to the chlor-alkali industry as well as water electrolysis. Iridium and ruthenium based oxides have long been the center of attention in this respect since they represent the industrial benchmark catalysts due to their exceptional activity and stability for these reactions.[1–3] Although the traditional approach in the development of oxide electrocatalysts aims primarily at the optimization of the oxide's activity, the issue of systematic selectivity control receives more attention in connection with the rational design of oxygen evolution catalysts and with the rational control of the electrocatalytic processes. Both anodic gas evolution processes are among the least thermodynamically favored redox reactions as shown by the rather high standard electrode potential of each reaction:[4]

$$O_2 + 4H^+ + 4e^- \rightleftharpoons 2H_2O \quad E_0 = 1.299\,V \qquad [1]$$

$$Cl_2(g) + 2e^- \rightleftharpoons 2Cl^- \quad E_0 = 1.358\,V \qquad [2]$$

Accepting the fact that the industrially relevant production of each gas requires a non-zero overpotential, one has to anticipate a simultaneous production of oxygen and chlorine at most potentials, making chloride contamination one of the more serious issues in water electrolysis.

The activity of ruthenium dioxide in both gas evolving reactions was systematically investigated by means of the density functional theory (DFT) based thermodynamic analysis. DFT analysis has been able to offer some insight regarding the competitive nature of both processes, confirming that the OER and CER are strongly correlated on rutile-type oxides.[5] According to the DFT analyses, the oxygen evolution reaction proceeds primarily through the formation of surface-confined hydroxo, oxo, or peroxo intermediate species on pentacoordinated Ru sites, also denoted as coordination unsaturated sites (*cus*).[6,7] Similarly, chlorine evolution on ruthenium dioxide is most likely to proceed via the formation of peroxo species bridging two adjacent *cus* sites ($O_{2,cus}$) which are subsequently subject to oxidative attack by Cl^-.[5] This theoretical description was recently challenged by Over et. al which assumes that *cus* confined oxo species are the most stable surface structure at the given conditions.[8]

The theoretical analysis also shows that the activity in chlorine evolution can be described with the same reaction descriptor as the oxygen evolution process, which in this case is the oxygen adsorption energy.[5] Despite the less favorable standard potentials, the theory confirms that the CER process is more facile than oxygen evolution and that the theoretical limiting overpotential required to drive CER is lower than that of OER in the whole range of oxygen binding energies.[6] This fact should lead to a complete suppression of the oxygen evolution activity on oxide surfaces even at moderate chlorine concentrations.

Keeping in mind the interdependence of the oxygen and chlorine evolution processes one may anticipate that the catalyst selectivity may be affected by controlling the oxygen binding energy to the oxide surface in a manner similar to that employed for controlling the oxygen evolution activity. Cationic substitution turns out to be a versatile approach in controlling the oxygen binding energy and has been demonstrated in the case of ruthenium dioxide modified with Ni,[9–12] Co,[11–17] Zn,[18] Sn,[19–21] and Fe.[22] Experiments combining voltammetric methods with differential electrochemical mass spectrometry (DEMS) have shown that the incorporation of the heterovalent cations generally affects the selectivity of the ruthenia-based catalyst in oxygen and chlorine evolution.[9,23,24] A general description of the relationships between the nature of the modified ruthenia-based catalyst and its selectivity is so far missing.

The issue of the oxide catalyst selectivity is addressed in this paper which also extends the previous studies on the selectivity of rutile-type oxides. In the current work we describe the synthesis of Mg-modified ruthenium dioxide containing various amounts of Mg and match their activity and selectivity in parallel oxygen and chlorine evolution with detailed structural correlations using extended X-ray absorption fine structure (EXAFS).

Experimental

Ruthenium dioxide and $Ru_{1-x}Mg_xO_2$ materials were synthesized using the spray-freezing freeze-drying method as outlined in reference 25. Aqueous solutions (8 mM) were prepared from ruthenium (III) nitrosylnitrate (31.3% Ru, Alfa Aesar) and magnesium acetate tetrahydrate (Puratronic®, 99.997% metals basis, Alfa Aesar) in 100 mL of Millipore H_2O. The solutions were then sprayed into liquid N_2 to create fine ice particles. The resulting ice slurry was transferred to an aluminum tray precooled with liquid N_2 and placed in the freeze dryer (FreeZone Triad Freeze Dry System 7400030, Labconco) precooled to −30°C. The pressure was decreased to approximately 1.0 Pa and the temperature was ramped according to the following program: −30°C (2h), −25°C (5h) −20°C (6h), −15°C (5h), 30°C (4h). Afterwards, the resulting powder was annealed in the furnace at 400°C for one hour.

*Electrochemical Society Fellow.
**Electrochemical Society Active Member.
zE-mail: Petr.Krtil@jh-inst.cas.cz

Crystallinity and phase purity of the prepared materials was checked using a Rigaku Miniflex 600 powder X-ray diffractometer with $Cu_{K\alpha}$ radiation. Morphology of the synthesized catalysts was characterized using a Hitachi S4800 scanning electron microscope (SEM) and a Nanotrace EDX detector (Thermo Electron) was used to evaluate the average sample compositions by X-ray energy dispersive spectroscopy. Particle size was evaluated by analyzing SEM images and averaging the size of 300 randomly chosen particles.

EXAFS spectra were measured at the Photon Factory synchrotron of the High Energy Accelerator Organization (KEK) in Tsukuba, Japan. The spectra were measured in transmission mode at the Ru K edge at beam-line AR-NW10A (Si(311) monochromator); the Mg K absorption edge was measured in total electron yield mode at the BL-11A beam-line (grazing incidence monochromator). Ru K scans extended to 20 $Å^{-1}$ and Mg K data were limited to 15 $Å^{-1}$. Each spectrum was recorded at four different scanning step sizes: the pre-edge region from 500 to 50 eV was scanned in 6.5 eV steps to enable background subtraction; in the 50 eV pre-edge and 100 eV post-edge range a step size of 0.4–0.5 eV was used to acquire the XANES part of the spectra, while a 2.5–3.0 eV and 7.0 eV scanning step was maintained in the post-edge regions of 100–500 eV and above 500 eV, respectively.

All data handling pre-requisite to the local structure refinement of the extended X-ray absorption fine structure (EXAFS) functions (i.e., normalization, smoothing and background subtraction, the Fourier transforms of the spectra and windowing) was done in the IFEFFIT software package.[26] The photoelectron wave vector k for the Fourier transform of spectra was kept within the range of $k = 3$–14 $Å^{-1}$ for Ru-EXAFS and $k = 3$–12 $Å^{-1}$ for Mg-EXAFS. The k-weighting factor of 2 was applied. For the analysis of the local structure of $Ru_{1-x}Mg_xO_2$ materials a full-profile refinement of the EXAFS spectra by non-linear least squares (NLLS) minimization in the R-space with a k-weighting factor equal to 2 was carried out using the Artemis NLLS module of the IFEFFIT package. The theoretical model was generated using FEFF6.2 library.

The X-ray photoelectron spectra (XPS) of the prepared materials and of the electrodes which were used in electrochemical experiments were measured using a modified ESCA 3 MkII multitechnique spectrometer equipped with a hemispherical electron analyzer operating in the fixed transmission mode. Al Kα radiation was used for electron excitation. The binding energy scale was calibrated using the Au 4f7/2 (84.0 eV) and Cu 2p3/2 (932.6 eV) photoemission lines. The spectra were collected at a detection angle of 45° with respect to the macroscopic surface normal. The studied materials were characterized using survey scan spectra and high resolution spectra of overlapping Ru 3d + C1s photoelectrons, Ru 4s, Mg 2s, O 1s photoelectrons and Mg $KL_{23}L_{23}$ Auger electrons. The spectra were curve fitted after subtraction of Shirley background using the Gaussian−Lorentzian line shape and nonlinear least-squares algorithms. Quantification of the elemental concentrations was accomplished by correcting the photoelectron peak intensities for their cross sections and for the analyzer transmission function. The typical error of quantitative analysis by XPS is ~10%.[27]

The electrocatalytic activity and selectivity in the oxygen evolution and chlorine evolution reactions were evaluated using a combination of potentiostatic experiments with differential electrochemical mass spectrometry (DEMS). Working electrodes were prepared from water and isopropanol based catalyst suspensions by sedimentation on Ti mesh (Goodfellow, 20% open area). Catalyst suspensions were prepared by mixing 10.0 mg RuO_2 or $Ru_{1-x}Mg_xO_2$ with 2.0 mL millipore H_2O and 2.0 mL isopropyl alcohol with subsequent homogenization in an ultrasonic bath and drop cast onto the Ti mesh current collector. The electrodes were dried in air at 60°C repeatedly until the desired catalyst loading (1–2 mg cm^{-2}) was obtained. Electrodes were annealed at 400°C in air for 2 hours to stabilize the catalyst layer. The measured current values were normalized with respect to the actual surface area based on the known mass of the catalyst and particle size based specific surface area.

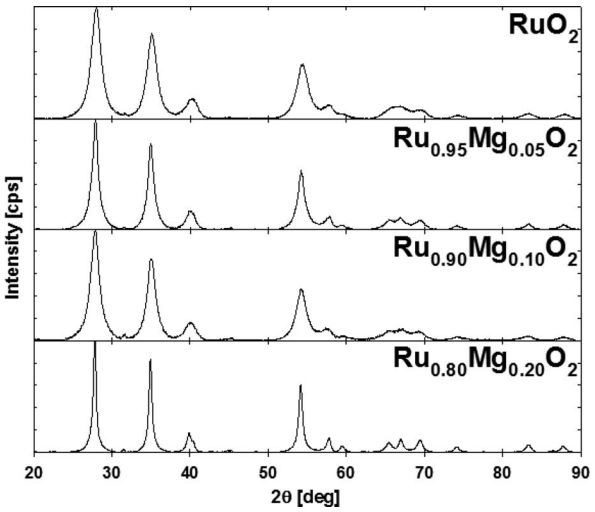

Figure 1. Powder X-ray diffraction patterns for nanocrystalline RuO_2 and $Ru_{1-x}Mg_xO_2$ after annealing in air for 1 hour at 400°C.

Electrochemical measurements were performed in a three electrode arrangement in a home-made Kel-F single compartment cell using a Pt auxiliary electrode and sat. Ag/AgCl reference electrode in 0.1 M $HClO_4$. The reference electrode itself was placed outside the cell and to avoid chloride leakage; the conductive connection of the reference electrode was achieved by a Luggin capillary. The potential of the working electrode in all experiments was controlled using a PAR 263A potentiostat. The DEMS apparatus consisted of a Prisma™ QMS200 quadrupole mass spectrometer (Balzers) connected to a TSU071E turbomolecular drag pumping station.

Results and Discussion

XRD, XPS and SEM characterization.— X-ray diffraction patterns for the synthesized materials are shown in Figure 1. The recorded patterns conform to a single phase tetragonal structure of the rutile-type as in RuO_2 (PDF file #431027). The incorporation of Mg into the rutile structure results in a change of the unit cell parameters which can be evaluated from the diffraction patterns. Assuming the oxidation state of Mg in the prepared material to be II, its incorporation into the RuO_2 framework should results in a slight expansion of the unit cell volume in the Mg-doped ruthenia (anticipating Mg to maintain octahedral coordination) due to the slightly larger ionic radius of the divalent magnesium (0.72 Å) with respect to that of the tetravalent ruthenium (0.62 Å).[27] This trend, however, is not experimentally encountered (see Table I). Incorporation of magnesium leads to an expansion of the lattice parameter a (which increases monotonously with

Table I. Results of the analysis of the powder diffraction data of the $Mg_xRu_{1-x}O_2$ catalysts.

Sample	a [Å]	c [Å]	V [$Å^3$]	Coherent domain size [nm]	Particle size [nm]	Strain (%)
RuO_2	4.454(15)	3.21(8)	63.68	4.3	9.6 ± 3.0	1.0(3)
$Ru_{0.95}Mg_{0.05}O_2$	4.478(13)	3.12(2)	62.56	5.9	5.3 ± 1.4	0.7(4)
$Ru_{0.90}Mg_{0.10}O_2$	4.505(3)	3.105(4)	63.02	4.6	5.0 ± 1.3	1.0(5)
$Ru_{0.80}Mg_{0.20}O_2$	4.509(3)	3.108(3)	63.19	12.0	5.5 ± 1.8	0.3(2)

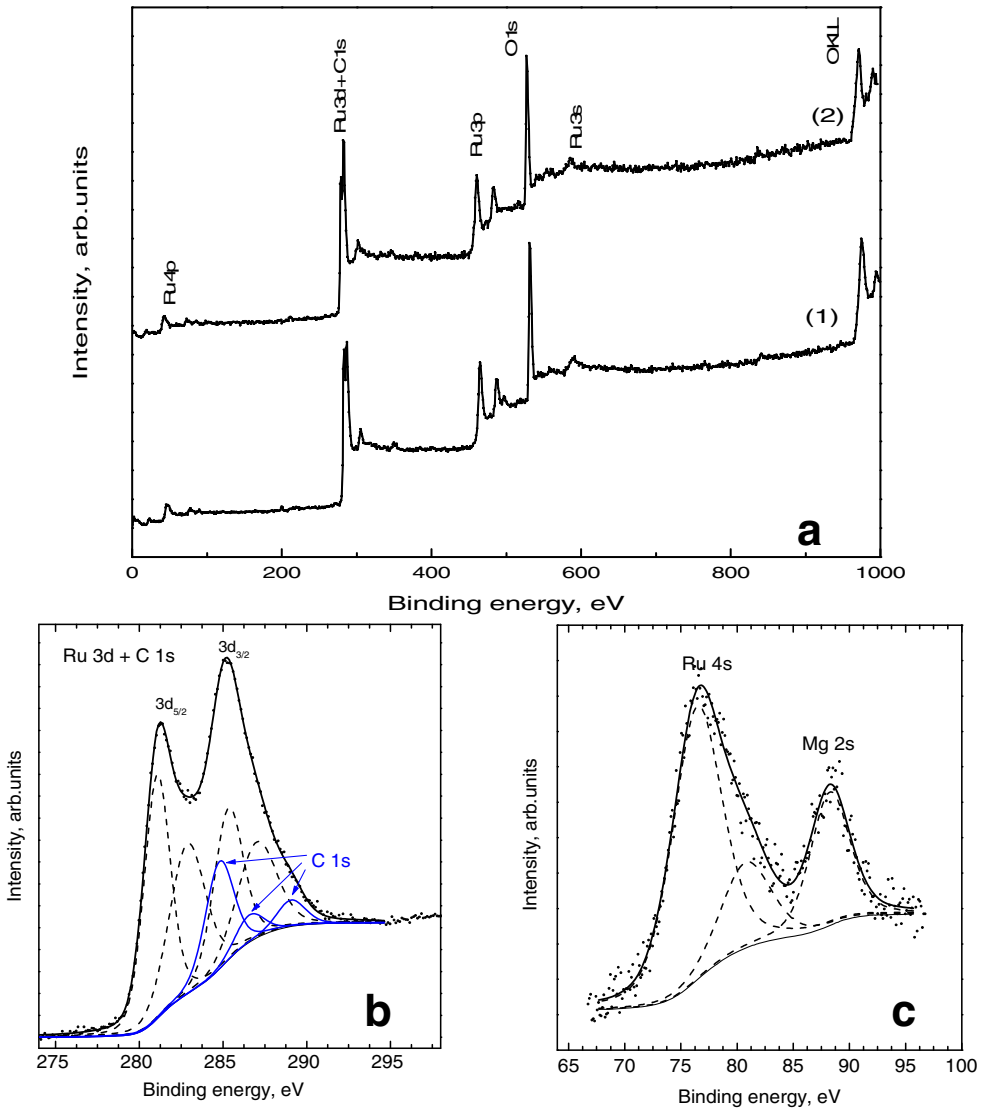

Figure 2. Survey scans (a) of $Ru_{0.8}Mg_{0.2}O_2$ before (1) and after (2) electrochemical experiments. Panes (b) and (c) contain fitted high resolution spectra of Ru 3d + C 1s (b) and Ru 4s + Mg 2s photoelectrons, respectively. The high resolution spectra of the $Ru_{0.8}Mg_{0.2}O_2$ after electrochemical experiments do not show significant differences from those plotted in panes (b) and (c).

increasing Mg content) and is accompanied by a significant shortening of the lattice parameter *c*, which further decreases with increasing Mg content. Although the unit cell volume of Mg-modified materials increases with increasing Mg content, its concentration dependent increase does not compensate for the initial decrease in unit cell volume associated with the incorporation of Mg. Similar unit cell shortening in the [001] direction has been previously reported for Ni-doped ruthenia and can be taken as an indicator that Mg is not evenly distributed in the resulting material.[10] The observed trend in the unit cell volume may also be interpreted in terms of the Mg local environment, specifically that of the oxygen coordination number with increasing Mg content. Such an interpretation should be, however, supported by local structure data based, e.g. on X-ray absorption spectroscopy. It needs to be noted that this change should be most pronounced in materials with a low magnesium content ($x < 0.1$). The single phase nature of the recorded XRD patterns suggests that the actual chemical composition agrees with the projected composition. The magnesium seems to be homogeneously distributed between bulk and surface of the nanoparticles as evidenced by the XPS-based surface composition and projected average composition (see Fig. 2 and Table II). This agreement is, however, weakened by the fact that the Mg XPS data are not available for samples with lower Mg content lower than 0.2.

Table II. XPS based surface metal content in $Ru_{0.8}Mg_{0.2}O_2$.

Sample	X_{Ru}	X_{Mg}
As synthesized	0.80	0.20
after electrochemistry	0.79	0.21

The relatively broad diffraction peaks are compatible with the anticipated nanocrystalline character of the materials. The average coherent domain size of the prepared materials can be approximated using the Scherrer formula:

$$D_i = \frac{\lambda}{\beta_i cos\theta_i} \quad [3]$$

where D_i is the size of the crystallite domain, λ is the wavelength of the incident radiation ($Cu_{K\alpha}$ = 1.540598 Å), β_i is the width of the diffraction peak at half maximum intensity measured in radians, and θ_i is the diffraction angle. The diffraction peak analysis yields an average coherent domain size ranging between 4 and 12 nm (see Table I). The nanocrystalline nature of the prepared materials is also confirmed in the SEM micrographs (see Fig. 3). Regardless of the

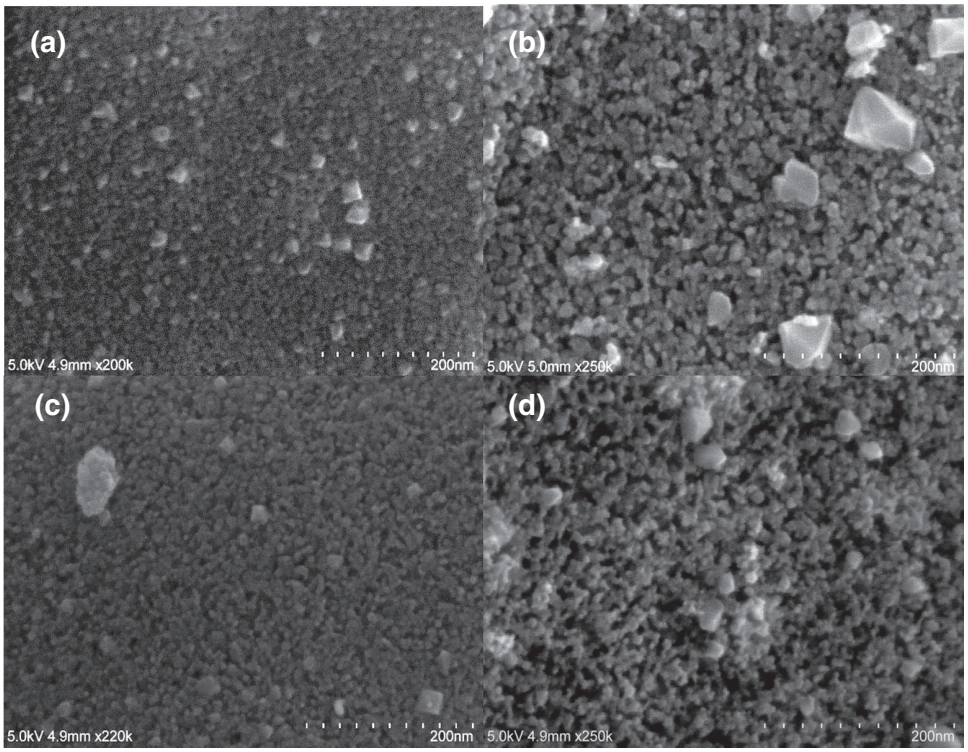

Figure 3. SEM images of nanocrystalline (a) RuO_2, (b) $Ru_{0.95}Mg_{0.05}O_2$, (c) $Ru_{0.90}Mg_{0.10}O_2$, and (d) $Ru_{0.80}Mg_{0.20}O_2$ after annealing in air for 1 hour at 400°C.

actual composition, the Mg-doped ruthenia forms isometric crystals with an average size of approximately 5 nm (see Table I) complemented with larger particles of approximately 40 nm. The coarse 40 nm particles are, however, significantly less represented. Despite the actual underrepresentation of the coarse nanoparticles, they form the principal diffracting regions controlling the shape of the diffraction peaks, particularly in the material containing 20% Mg. This fact results in a significant discrepancy between the coherent domain size and the actual particle size such that the coherent domain size exceeds the particle size based on analysis of the micrographs.

Local structure characterization.— Information complementary to the diffraction is extractable from the X-ray absorption spectra measured on the Ru and Mg K edges (See Fig. 4). The experimentally observed Ru K edge position of the Mg doped ruthenia is not sensitive to the actual Mg content and is equal to 22133 eV. This value agrees well with that reported for ruthenium dioxide in the literature.[9,13] The corresponding EXAFS functions as they are presented in Fig. 4a are also insensitive to the magnesium content and agree qualitatively with the Ru EXAFS functions reported for doped ruthenia previously.[10] The observed behavior is generally compatible with the non-homogeneous distribution of magnesium in the RuO_2 matrix, resulting in the formation of Mg enriched clusters, the nature of which may depend on the overall Mg content. The magnesium K edge position in the X-ray absorption spectra of the Mg doped ruthenia shifts with increasing Mg content from ca. 1310 eV (material containing 5% Mg) to 1308 eV (material containing 20% Mg). The Mg content-dependent shift of the Mg K edge position may be interpreted either in terms of a change in oxidation state or in terms of a change in local structure. The observed Mg absorption edge values, primarily those for the materials with low total Mg content, exceed that observed for the MgO standard (1309 eV) and could be formally assigned to an increase in the oxidation state. Keeping in mind the alkaline earth nature of magnesium, however, the assignment of the observed trend in the position of the Mg absorption edge energy to the overall effects of bonding

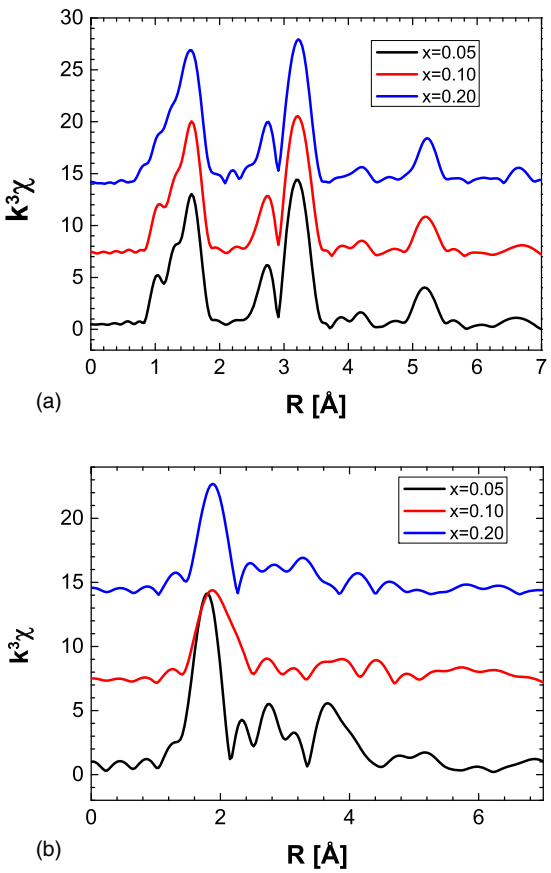

Figure 4. EXAFS functions extracted from the X-ray absorption spectra of the $Ru_{1-x}Mg_xO_2$ ($0 < x < 0.2$) measured on the (a) Ru K edge and (b) Mg K edge. Actual Mg content is shown in the Figure legend.

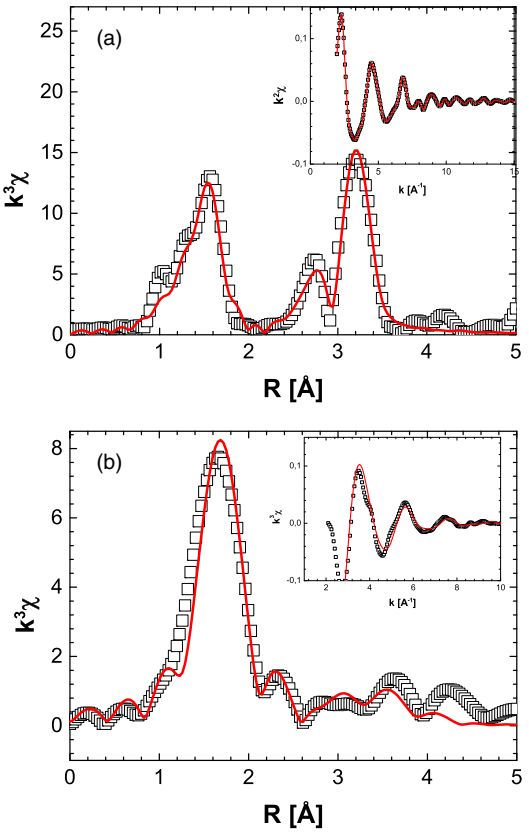

Figure 5. (a) A typical example of the non-linear least square fit of the Ru EXAFS function of $Ru_{0.95}Mg_{0.05}O_2$. The square symbols represent the experimental data, the red line denotes the best fit.; (b) A typical example of the non-linear least square fit of the Mg EXAFS function of $Ru_{0.90}Mg_{0.10}O_2$. The square symbols represent the experimental data, the red line denotes the best fit.

arrangements in the vicinity of Mg seems to be more likely. The Mg EXAFS functions obtained from the Mg K edge X-ray absorption spectra, in contrast to the Ru EXAFS functions, are affected by the actual Mg content (see Fig. 4b).

The Ru EXAFS functions can be refined assuming a structural model based on ruthenium dioxide with a rutile structure. A typical example of the refinement for the Ru EXAFS functions is plotted in Fig. 5a; the results of the EXAFS function refinement are summarized in Table III. It may be concluded that the bonding arrangements in the ruthenium environment are essentially unperturbed by the incorporation of Mg. The Ru-O as well as the Ru-Me (Me = Ru or Mg) bonding distances and the Ru coordination arrangements do not differ significantly from those of pure ruthenium dioxide. The presence of Mg in the direct neighbor metal positions with respect to the absorbing ruthenium is lower than that corresponding to the average chemical composition.

The refinement of the Mg EXAFS functions is only possible for the materials containing at least 10% Mg in the cationic positions. The quality of the XAS spectra for materials with lower Mg content was not sufficient for the full refinement. The refinement of the Mg local structure using a rutile-type structural model does not give convergent results as can be seen by the absence of the characteristic cation-cation interactions corresponding to bonding distances of ca. 3.1 and 3.5 Å. It ought to be stressed that resolved scattering due to the cation-cation interactions with a bonding distance in the range of 3 to 4 Å is characteristic for most of the binary and ternary oxide structural types and its absence suggests a rather complex and disordered nature of the Mg local environment. The actual Mg-O bonding distances in the first coordination shell increase with increasing Mg content from ca. 2.00 (x = 0.1) to 2.07 Å (x = 0.2). This trend reflects a gradual relaxation

Table III. a. Results of the NLLS fit of the EXAFS functions obtained from the Ru K edge X-ray absorption spectra of the $Mg_xRu_{1-x}O_2$ (0 < x < 0.2) catalysts. CN denotes the coordination number and d stands for the bonding length. b. Theoretically conceived local structures of the Mg in rutile and ilmenite type MgRuO oxides and results of the NLLS fit of the EXAFS functions obtained from the Mg K edge X-ray absorption spectra of the $Mg_xRu_{1-x}O_2$ (0 < x < 0.2) catalysts. The theoretically conceived data are given in italics. Symbol assignment are the same as in the case of Table IIIa.

Sample	Bond	CN	Error	d [Å]	Error
		a			
$Ru_{0.95}Mg_{0.05}O_2$	Ru-O	2.0	0.2	1.937	0.006
		4.0	0.4	1.982	0.006
	Ru-Ru	1.8	0.4	3.100	0.010
	Ru-O	4.0	0.4	3.410	0.007
	Ru-Ru	7.1	1.5	3.552	0.006
	Ru-Mg	0.8	0.9	3.552	0.006
$Ru_{0.90}Mg_{0.10}O_2$	Ru-O	2.0	0.2	1.938	0.007
		4.0	0.3	1.982	0.007
	Ru-Ru	2.1	0.6	3.101	0.009
	Ru-O	4.0	0.3	3.408	0.007
	Ru-Ru	6.3	2.0	3.556	0.008
	Ru-Mg	1.7	1.5	3.556	0.008
$Ru_{0.80}Mg_{0.20}O_2$	Ru-O	2.0	0.3	1.937	0.008
		4.0	0.6	1.981	0.008
	Ru-Ru	2.2	0.8	3.101	0.010
	Ru-O	4.0	0.6	3.407	0.008
	Ru-Ru	6.5	2.1	3.557	0.009
	Ru-Mg	1.5	1.5	3.667	0.009
		b			
Rutile	*Mg-O*	*2*		*1.94*	
		4		*1.98*	
	Mg-Ru	*2*		*3.14*	
	Mg-O	*4*		*3.41*	
	Mg-Ru	*8*		*3.55*	
Ilmenite	*Mg-O*	*3*		*1.95*	
		3		*2.17*	
	Mg-Ru	*1*		*3.01*	
		3		*3.05*	
	Mg-O	*3*		*3.40*	
	Mg-Ru	*6*		*3.36*	
$Ru_{0.90}Mg_{0.10}O_2$	Mg-O	6.1	0.5	2.00	0.02
	Mg-Ru	2.9	0.9	3.08	0.03
	Mg-Mg	4.0	1.4	3.38	0.03
	Mg-O	5.1	1.2	3.315	0.08
	Mg-Ru	4.0	0.5	3.55	0.03
$Ru_{0.80}Mg_{0.20}O_2$	Mg-O	6.5	1.2	2.07	0.05
	Mg-Ru	2.2	0.7	2.88	0.06
	Mg-Mg	1.8	0.5	3.07	0.04
	Mg-O	4.0	1.0	3.52	0.07
	Mg-Ru	1.5	0.8	3.37	0.04
		2.0	0.8	3.56	0.04

of the Mg environment from the bonding arrangements native to rutile framework of RuO_2. The trend in the Mg-O bonding distance reflects the general incompatibility of Mg with the RuO_2 environmental confinement which brings substantial strain to the material and has to be stabilized by the small size of the Mg cluster as well as the overall particle size. The Mg-O bond length observed in materials with low overall Mg content is comparable with that of the Ru-O bond in the ruthenium dioxide. It is, however, also approximately 0.1 Å shorter that the Mg-O bonding distance in the thermodynamically stable cubic magnesium oxide (2.12 Å). The refined Mg-O bonding distance trend seems to be in accordance with the observed shift in the Mg absorption edge toward higher energies. It is, however, unrealistic to assign the observed behavior to the removal of a third electron from Mg and we attribute the experimental behavior rather to the strain imposed by the adjacent Ru-rich rutile-type matrix.

A full refinement of the Mg EXAFS functions requires the formulation of a convenient structural model reflecting the overall chemical composition of the prepared materials. Since Ru and Mg do not form stable double oxides one has to base an applicable local structure model on the double oxides existing in the Mg-Ti-O ternary system.[28] Although magnesium and titanium form two stable ternary oxides conforming to the spinel and ilmenite structural models, the absence of the pronounced scattering between 3 and 4 Å seems to disagree with both possible structural models for the Mg EXAFS function refinement (see Fig. 5b).

A satisfactory fit of the experimental data can be achieved assuming that the local environment of Mg bears features of both the ruthenia host (rutile structural model) and of the stable ternary Mg-Ru-O oxide conforming to an ilmenite structural model. Typical result of the full refinement for the Mg EXAFS functions is shown in Fig. 5b; the parameters of the refinement are included in Table III. As shown by the parameters of the refinement summarized in Table III, the observed increase in the Mg-O bonding distance with increasing overall Mg content from ca. 2.00 to ca. 2.07 Å can therefore be viewed as a relaxation from when the Mg originally confined in the rutile-like oxygen coordination gradually relaxes to a local structure similar to that in stable Mg oxide(s).[29] The refined EXAFS functions do not reflect any change in the Mg-O coordination suggested by the composition dependence of the unit cell volume. The possibility of a change in the Mg-O coordination, specifically at low Mg contents, however, cannot be ruled out since the EXAFS functions of $Ru_{1-x}Mg_xO_2$ with $x < 0.10$ are not available.

It needs to be stressed that the Mg-O bonding distance in all prepared materials remains shorter than that in Mg-O or Mg-Ti-O and the Mg local environment remains rather strained. The cationic arrangement also shows a gradual development between bonding distances and coordination numbers characteristic for a rutile-like structure ($Ru_{0.9}Mg_{0.1}O_2$) and those approaching the values expected for ilmenite ($Ru_{0.8}Mg_{0.2}O_2$). It needs to be stressed that although the nearest cationic coordination in the later material starts to resemble the ilmenite, there still remain observable cation–cation interactions characteristic of a rutile-like structure. This behavior is not surprising since both structural types are related as it was shown, e.g. in reference 18.

Electrochemical and DEMS measurements.— The Mg doped materials are active catalysts for both oxygen and chlorine evolution. The results of the electrochemical characterization are summarized in Figures 6–10. The incorporation of Mg into the rutile structure apparently decreases the activity of the ruthenia-based catalysts for the oxygen evolution process (see Fig. 6). Such behavior contradicts that of the Ni or Co containing analogs.[10,13] The observed behavior seems to reflect the fact that the cation perturbing the local structure of the catalyst is itself catalytically inactive (i.e. cannot enter redox reactions and become a binding site of the reaction intermediates). The decrease in the oxygen evolution activity shows, however, a non-monotonous dependence on the actual Mg content with a maximum activity observed for the material with an overall Mg content of $x = 0.10$. This behavior cannot be directly linked with the refined local structure and its explanation will most likely need to employ advanced theoretical approaches.

The overall activity of the Mg modified ruthenia and pure ruthenia toward parallel oxygen and chlorine evolution can be seen in Figure 7. The measured faradaic current shows a linear dependence on the chloride concentration in the electrolyte solution. The increase in the overall activity is also accompanied with a significant change in the material's selectivity. While approximately 30% of the charge being passed at a concentration of 300 mM Cl^- can be attributed to oxygen evolution on the non-doped ruthenia (see Fig. 8), in the case of the Mg doped materials the yield of the oxygen drops below 20% for a chloride concentration of 50 mM and the chlorine evolution becomes practically quantitative at higher chloride concentrations.

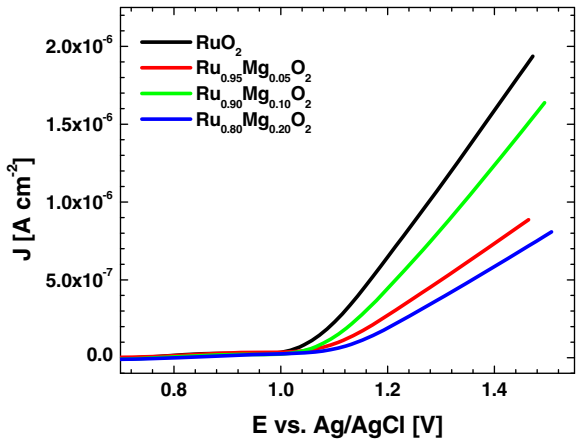

Figure 6. Linear scan voltammograms of the oxygen evolution on $Mg_xRu_{1-x}O_2$ electrodes ($0 < x < 0.2$) recorded in 0.1 M $HClO_4$ at a polarization rate of 5 mV s^{-1}. The curve assignment is given in the Figure legend.

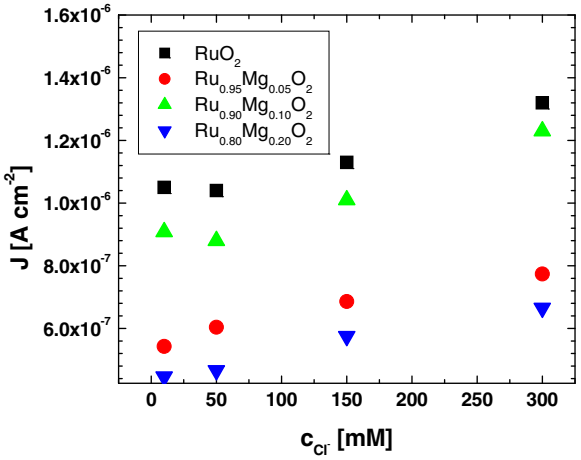

Figure 7. Chloride concentration dependence of the overall current response of $Mg_xRu_{1-x}O_2$ electrodes to anodic polarization in chloride containing acid media. The presented values correspond to potentiostatic experiments at 1.25 V vs. Ag/AgCl. The data correspond to the situation after 3 minutes at the given potential.

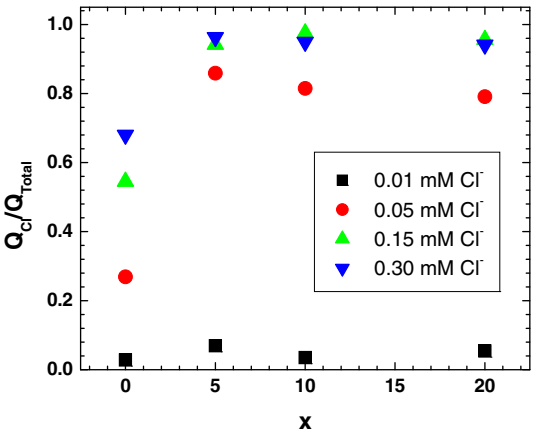

Figure 8. Composition dependence of the Mg doped ruthenia selectivity toward chlorine evolution. The data correspond to potentiostatic experiments at 1.25 V (Ag/AgCl). The actual chloride concentrations are given in the Figure legend. The data correspond to the situation after 3 minutes at the given potential.

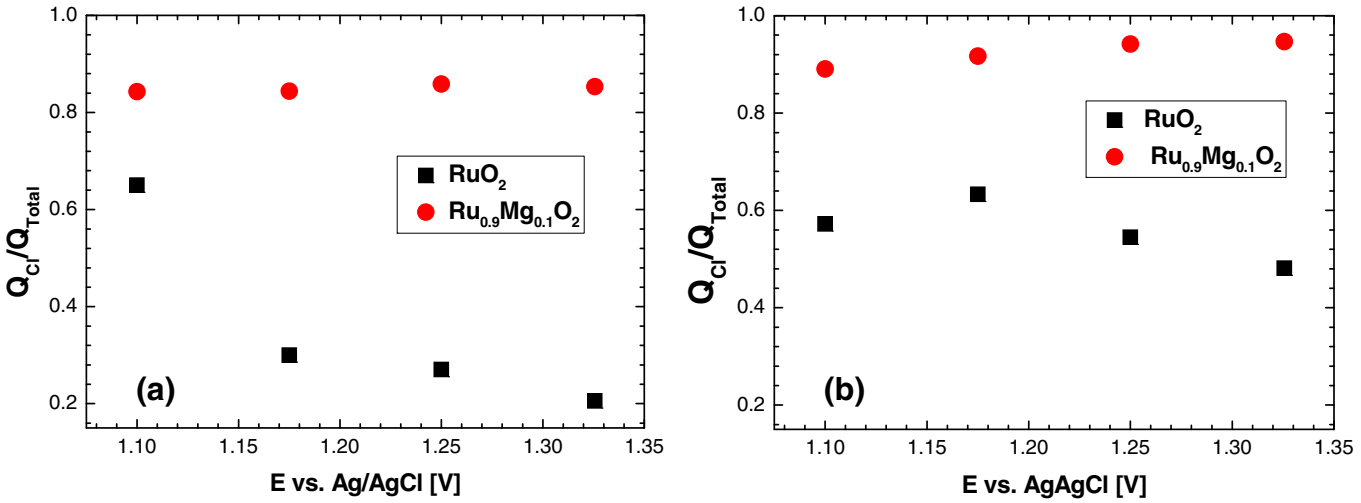

Figure 9. Potential dependence of the Mg doped ruthenia selectivity toward chlorine evolution. The data were extracted from potentiostatic experiments in 0.1 M $HClO_4$ containing (a) 10mM NaCl and (b) 50mM NaCl after 3 minutes at 1.25 V (Ag/AgCl).

The selectivity of the Mg modified ruthenia toward chlorine evolution seems to be little affected by the catalyst's composition; at higher chloride concentrations the selectivity is also independent of the electrode potentials. A potential dependence of the catalyst's selectivity remains, however, observable at low to medium chloride concentrations (10 to 50 mM) when all catalysts seem to favor the chlorine evolution at lower overpotentials. The selectivity of non-doped catalysts, however, changes toward oxygen evolution at more positive potentials (see Fig. 9). Detailed information on the nature of the selectivity of both Mg doped as well as non-doped ruthenia can be obtained by analyzing the time courses of the oxygen and chlorine evolution at constant potential in solution containing 10 mM of sodium chloride (see Fig. 10). The DEMS signals corresponding to both anticipated reaction products start to rise simultaneously after the application of the potential step and chlorine evolution signal attains a steady state value after 10 and 40 s. These steady state values reflect equalization of the

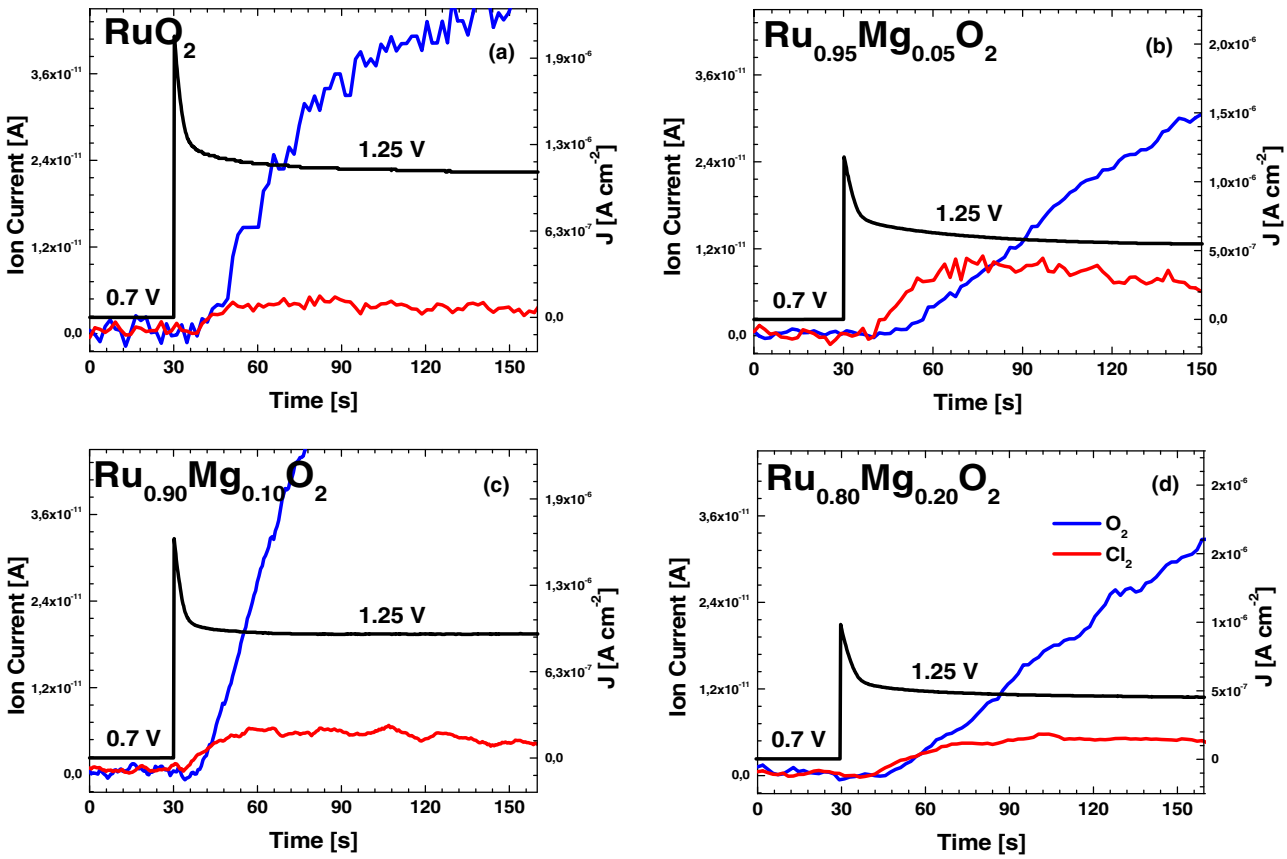

Figure 10. Time course of DEMS-based signals of potentiostatically generated oxygen (blue) and chlorine (red) for (a) RuO_2, (b) $Ru_{0.95}Mg_{0.05}O_2$, (c) $Ru_{0.90}Mg_{0.10}O_2$, and (d) $Ru_{0.80}Mg_{0.20}O_2$. Signals were recorded in 0.1 M $HClO_4$ containing10 mM NaCl; the potential perturbation corresponded to a step from 0.70 V to 1.25 V vs. Ag/AgCl.

rate of chlorine production and its removal into the DEMS apparatus. The fact that the chlorine evolution signal attains a steady state value before the oxygen evolution signal indicates that the oxygen evolution process does not affect the rate of chlorine evolution. This type of behavior contradicts the assumed strict competition of both anodic processes for the same active sites at the catalyst's surface. The chlorine and oxygen evolution processes apparently use different surface structures. The obtained data also suggest that the chlorine evolution pathway is kinetically less hindered than that used for oxygen evolution. It needs to be noted that the active sites used in chlorine evolution can also catalyze the oxygen evolution process if chlorine evolution becomes transport limited.

The conditions of the electrochemical experiments are generally incompatible with the sample composition in general. To establish a general validity of the electrochemical data all experiments were run with fresh electrodes and the duration of the experiments was kept short and never exceeded 1000 s. The surface composition after the electrochemistry as reflected in the XPS spectra agrees well with the initial one (see Tables I and II). Although this fact validates the relevance of the presented electrochemical data it does not allow to make any predictions related to the practical suitability of the prepared materials in industry-like applications where the catalyst should exhibit stability on significantly longer time-scales ($\sim 10^8$ s).

Discussion.— Traditionally, the theoretical description of the oxygen evolution process on rutile-type ruthenium dioxide designates the active sites as transition metal atoms in so-called *cus* positions. The significant enhancement of the oxygen evolution activity achieved by the modification of the rutile structure with Ni or Co is then attributed to the activation of the *bridge* sites for a proton transfer by incorporation of the additional transition metal.[30] The incorporation of alkaline earth metal cations, such as Mg, however, is unlikely to improve the catalytic activity of the rutile structure even if present in the *cus* positions. The catalytic cycle for oxygen evolution formally requires the active metal cations to be oxidizable if they should contribute to the overall activity. This can be hardly achievable given the oxidation state of Mg in the prepared materials. This fact is reflected in the drop in oxygen evolution activity which therefore results from a decrease in the available active Ru *cus* sites via dilution effect.

The link between the selectivity of parallel oxygen and chlorine evolution with the catalyst's local structure has not been established. Although the selectivity of similar systems, e.g. Co[13] or Ni,[9] doped ruthenia has been experimentally assessed in parallel oxygen and chlorine evolution, the presented results were interpreted mainly in terms of morphology rather than local structure.[24] Although the theory suggests that superiority of the chlorine evolution should be structure insensitive, the experimental studies on Ni, Co, and Zn[18] doped ruthenia are rather equivocal. In this regard one may consider two types of structures attributable to dopant incorporation. The first type represents Ni and Co doped ruthenia which generally form surface structures characterized by isolated or stacked Ni and Co cations which reside in a strained rutile-like environment.[9,13] The stacking of the dopant atoms along the *c* axis shifts the selectivity toward chlorine evolution.[9] Breaking the dopant arrangements along the *c* axis, e.g. due to shear plane formation,[10] shifts the selectivity toward oxygen evolution.[9] The Zn doped materials, on the other hand, form local structures characterized by partially or fully broken stacking of *cus* and *bridge* sites[18] and their unusual selectivity toward oxygen evolution was previously attributed to the structural hindrance of forming peroxo bridges between adjacent *cus* sites.

The Mg doped materials, from a structural point of view, represent a transition in the local structure from where the dopant stacking in the *bridge* and *cus* sites is essentially unperturbed (characteristic for pure RuO_2 and for Ni and Co doped ruthenia) to a structure containing dopant enriched ilmenite-like inclusions characteristic for Zn doped ruthenia. A purely structural comparison, therefore, suggests the electrocatalytic behavior of the Mg doped ruthenia to fall between that of the non-doped and Zn doped ruthenia. This trend seems to be fully reflected in oxygen evolution data when both Zn^{2+} and Mg^{2+} suppress the activity in the oxygen evolution. The adherence of the behavior of Mg doped ruthenia observed in chloride containing solutions to the theory predictions is less pronounced. The Mg doped materials show a preference for chlorine evolution which peaks for the material featuring about 5% Mg in cationic positions (see Fig. 8). Although the detailed local structure information for this material is missing it may be envisaged that this material shows the closest similarity to the non-doped ruthenia. The moderate selectivity shift toward oxygen evolution observed for the materials with higher Mg content reflects the development of the catalysts' local structure toward ilmenite-type inclusions. Breaking the stacking of cationic positions decreases the possibility to form peroxo bridges between adjacent *cus* sites which were proposed to be primary chlorine evolution active sites.[18] The shift of the selectivity of Mg doped ruthenia toward oxygen evolution, however, lags behind that of the Zn doped ruthenia for chlorine evolution. The precise nature and functionality of the chlorine evolution active sites in Mg doped ruthenia cannot be, however, described experimentally with sufficient precision and needs to be backed with complementary DFT-based studies modeling both surface stability and activity of doped ruthenia based catalysts.

Conclusions

Nanocrystalline Mg doped ruthenium dioxide catalysts were prepared by the spray-freezing freeze-drying technique. Regardless of the average chemical composition, the prepared materials are of nanocrystalline character with an average particle size of approximately 5 nm. Despite the larger radius of the Mg cation compared with the tetravalent ruthenium cation, the observed decrease in the unit cell volume suggests a nonhomogeneous distribution of Mg in the structure with a local environment corresponding to that of a disordered ilmenite structure. Such an arrangement is also supported by the analysis of the Mg EXAFS functions. The incorporated Mg apparently exists in a significantly strained environment as shown by the shift in the Mg K absorption edge energies as well as the unusually short Mg-O bonding distances which do not exceed 2.07 Å. The prepared materials are active in both oxygen as well as in chlorine evolution reaction. While the oxygen evolution activity is suppressed on Mg doped ruthenia, the chlorine evolution is enhanced compared to the conventional ruthenia.

Acknowledgments

This work was supported by the European Commission within the Initial Training Network ELCAT (Project No. 214936). The synchrotron measurement time was provided by the KEK of Japan within the projects 2013R-35 and 2009R-29.

References

1. S. Trasatti, *Electrochim. Acta*, **45**, 2377 (2000).
2. S. Trasatti, *Electrochim. Acta*, **29**, 1503 (1984).
3. L. D. Burke, O. J. Murphy, J. F. O'Neill, and S. Venkatesan, *J. Chem. Soc., Faraday Trans. 1*, **73**, 1659 (1977).
4. A. J. Bard and L. R. Faulkner, *Electrochemical Methods: Fundamentals and Applications* (John Wiley & Sons, Inc., New York, 2001).
5. H. A. Hansen, I. C. Man, F. Studt, F. Abild-Pedersen, T. Bligaard, and J. Rossmeisl, *Phys. Chem. Chem. Phys.*, **12**, 283 (2010).
6. I. C. Man, H.-Y. Su, F. Calle-Vallejo, H. A. Hansen, J. I. Martinez, N. G. Inoglu, J. Kitchin, T. F. Jaramillo, J. K. Norskov, and J. Rossmeisl, *Chem. Cat. Chem.*, **3**, 1159 (2011).
7. J. Rossmeisl, Z.-W. Qu, H. Zhu, G.-J. Kroes, and J. K. Nørskov, *J. Electroanal. Chem.*, **607**, 83 (2007).
8. K. S. Exner, J. Anton, T. Jacob, and H. Over, *Electrochim. Acta*, **120**, 460 (2014).
9. K. Macounova, M. Makarova, J. Jirkovsky, J. Franc, and P. Krtil, *Electrochim. Acta*, **53**, 6126 (2008).
10. V. Petrykin, Z. Bastl, J. Franc, K. Macounova, M. Makarova, S. Mukerjee, N. Ramaswamy, I. Spirovova, and P. Krtil, *J. Phys. Chem. C*, **113**, 21657 (2009).
11. N. Krstajic and S. Trasatti, *J. Electrochem. Soc.*, **142**, 2675 (1995).
12. N. Krstajic and S. Trasatti, *J. Appl. Electrochem.*, **28**, 1291 (1998).
13. V. Petrykin, K. Macounová, M. Okube, S. Mukerjee, and P. Krtil, *Catal. Today*, **202**, 63 (2012).
14. L. M. D. Silva, J. F. C. Boodts, and L. A. DeFaria, *Electrochim. Acta*, **45**, 2719 (2000).

15. L. M. D. Silva, J. F. C. Boodts, and L. A. D. Faria, *Electrochim. Acta*, **46**, 1369 (2001).
16. L. M. D. Silva, L. A. D. Faria, and J. F. C. Boodts, *J. Electroanal. Chem.*, **532**, 141 (2002).
17. C. Hummelgård, R. K. B. Karlsson, J. Bäckström, S. M. H. Rahman, A. Cornell, S. Eriksson, and H. Olina, *Mater. Sci. Eng., B*, **178**, 1515 (2013).
18. V. Petrykin, K. Macounova, J. Franc, O. Shlyakhtin, M. Klementova, S. Mukerjee, and P. Krtil, *Chem. Mater.*, **23**, 200 (2011).
19. J. Gaudet, A. C. Tavares, S. Trasatti, and D. Guay, *Chem. Mater.*, **17**, 1570 (2005).
20. X. Wu, J. Tayal, S. Basu, and K. Scott, *Int. J. Hydrogen Energy*, **36**, 14796 (2011).
21. K. Xiong, Z. Deng, L. Li, S. Chen, M. Xia, L. Zhang, X. Qi, W. Ding, S. Tan, and Z. Wei, *J. Appl. Electrochem.*, **43**, 847 (2013).
22. K. Macounová, M. Makarova, J. Franc, J. Jirkovský, and P. Krtil, *Electrochem. Solid State Lett.*, **11**, F27 (2008).
23. M. Makarova, J. Jirkovský, M. Klementová, I. Jirka, K. Macounová, and P. Krtil, *Electrochim. Acta*, **53**, 2656 (2008).
24. V. Petrykin, K. Macounova, O. A. Shlyakhtin, and P. Krtil, *Angew. Chem.*, **49**, 4813 (2010).
25. Y. D. Tretyakov and O. A. Shlyakhtin, *J. Mater. Chem.*, **9**, 19 (1999).
26. M. Newville, *J. Synchrotron Radiat.*, **8**, 322 (2001).
27. D. Briggs and J.T. Grant in *Surface Analysis by Auger and X-ray Photoelectron Spectroscopy* (IM Publications and SurfaceSpectra Ltd.,Cromwell Press, Trowbridge, 2003), p. 326.
28. R. D. Shannon, *Acta. Cryst.*, **A32**, 751 (1976).
29. R. W. G. Wyckoff, *The Structure of Crystals* (Reinhold Publishing Corporation, New York, USA, 1935).
30. N. B. Halck, V. Petrykin, P. Krtil, and J. Rossmeisl, *Phys. Chem. Chem. Phys.*, **16**, 13682 (2014).